Proceedings of the Twenty-first (2011) International Offshore and Polar Engineering Conference
Maui, Hawaii, USA, June 19-24, 2011

ISBN 978-1-880653-96-8 (Set); ISSN 1098-6189 (Set); www.isope.org

Parallel Simulation of 3D Lid-driven Cubic Cavity Flows by Finite Element Method

Jifei Wang and Decheng Wan
State Key Laboratory of Ocean Engineering, School of Naval Architecture, Ocean and Civil Engineering, Shanghai Jiao Tong University
Shanghai, China

ABSTRACT

The fractional step finite element method and domain decomposition method are applied to parallel simulate the 3D lid-driven cubic cavity flows based on the open source codes PETScFEM. The Reynolds numbers (Re) between 1 and 10000 are considered, covering laminar and partly turbulent field. Primary eddy, secondary eddies, corner eddies, Taylor-Gortler-like (TGL) vortices and other cavity flow features are researched. At high Reynolds number, the mean and mean-root-square velocities statistics along the horizontal and vertical centerlines in the symmetry plane keep reasonable agreement with experiment data respectively. Parallel performance is also analyzed.

KEY WORDS: PETScFEM; 3D cavity flows; domain decomposition; parallel computation; TGL vortices; high Reynolds number.

INTRODUCTION

Lid-driven cavity flows are not only technologically important, but also they are of great scientific interest. These flows display many kinds of fluid mechanical phenomena, including corner eddies, Taylor-Gortler-like (TGL) vortices, transition, turbulence and so on. Simple geometrical settings and easily posed boundary conditions have made cavity flows become popular test cases for computational schemes.

As a classic benchmark, the 2D lid-driven cavity flows have been extensively studied with numerical methods. However, the pioneering experimental work of Koseff & Street and coworkers in the early 1980s clearly showed that cavity flows were inherently 3D in nature. With the increase of computing capability in recent years, the 3D lid-driven cavity problems have matured as a standard Re-dependent benchmark. Jiang *et al*. (1994), Wong *et al*. (2002) and many other researchers have investigated the lid-driven cubic cavity at low and moderate Reynolds number. Prasad & Koseff (1989) have studied the 3D lid-driven cavity flows at Re=3200, 5000, 7500, and 10000 with experimental methods, which improves the research of these problems at moderate and high Reynolds number with numerical methods. Zang *et al*. (1993) have applied finite volume method in a lid-driven cavity at Reynolds numbers of 3200, 7500, and 10000, showing agreement with the experimental data. Large eddy simulations (LES) have enjoyed popularity for turbulent flows. Bouffanais *et al*. (2007) and Shetty *et al*. (2010) have analyzed the lid-driven cubic cavity at high Reynolds numbers by LES. Direct numerical simulation (DNS) is also popular, which can be used for both laminar and turbulent flows. Leriche *et al*. (2006) and Hachem *et al*. (2010) have simulated the cubic cavity flows at moderate and high Reynolds numbers by DNS. As reviewed in Shankar *et al*. (2002), the flow fields of the lid-driven cubic cavity are laminar when Re<6000; transition to turbulence takes place in the range 6000<Re<8000, and sufficient partition of the fields are turbulent by Re=10000; TGL vortices can be observed in both unsteady laminar and turbulent flows.

It is difficult to obtain the solution of incompressible Navier-Stokes (NS) equations using classical finite element method. The mathematical analysis of the Stokes problem shows that the approximation spaces for velocity and pressure must satisfy a compatibility condition known as the *inf-sup* LBB (proposed by Ladyzhenskaya, Babuska and Brezzi) condition. This has the drawback that only some combination of interpolation spaces for velocity and pressure can be used. However, the fractional step method based on the Poisson projection can be used with spatial interpolations which do not satisfy the LBB condition. These methods are applied widely because of the computational efficiency. Guermond *et al*. (1998) have investigated the stability and convergence of fractional step method with equal order interpolations. It is shown that there is a lower bound for the time step for stability reason. Codina (2001) got the similar results and presented a stabilized fractional step finite element method. These results are used in this work.

Based on the open source codes PETScFEM, fractional step finite element method (FEM) with domain decomposition technique is applied for parallel simulation of 3D lid-driven cubic cavity flows. The numerical method is briefly introduced as follows: In the preprocessing, the computational domain is discretized by the regular mesh with the brick elements. The fractional step method is applied to decouple the incompressible Navier-Stokes system in three sub-steps. All these three sub-equations are discretized by finite element method with the equal order interpolation of the velocity and pressure in space. For the parallel computation, the whole mesh is decomposed to several non-overlapping sub-domains. All the sub-domains are computed at the same time. The information of the interface among the sub-domains is passed among the processors by MPI (Message Passing Interface). All the linear systems are solved by GMRES (Generalized Minimal RESidual) method with Jacobi preconditioner, which are carried out in PETSc (Portable, Extensible Toolkit for Scientific computation). With the numerical method described above, this paper parallel simulates the 3D lid-driven cubic cavity flows at different Reynolds numbers. The reliability and efficiency of the numerical method is validated at Re=1000. The velocity profile coincides with the reference values. The 3D streamlines, velocity vectors, pressure iso-surfaces, and vorticity iso-surfaces are presented. Then lid-driven cavity flows at low Reynolds numbers (1, 10, 100, and 400) are simulated to show the corner eddies, which indicate the intrinsic 3D property. Cavity flows at moderate Reynolds numbers (2000, and 3200) are simulated to observe the evolution of the TGL vortices. Finally cavity flows at high Reynolds number (10000) is simulated, which is partly turbulent. The mean and root-mean-square velocity statistics (Re=3200, 10000) are briefly presented, which keep reasonable agreement with the experiment data.

This paper is organized as follows: In the second section, the detailed numerical algorithms applied in this paper are presented. Then numerical results of 3D lid-driven cubic cavity flows at different Reynolds numbers are given. The parallel performance is also analyzed. The paper ends with a concluding remark.

NUMERICAL METHOD

Governing Equations

The Navier–Stokes equations governing incompressible viscous fluid flow in a domain Ω in a time interval $[0,T]$ are

$$\partial_t \boldsymbol{u} + \boldsymbol{u}\cdot\nabla\boldsymbol{u} + \nabla p - \nu\Delta\boldsymbol{u} = 0\,, \tag{1}$$

$$\nabla\cdot\boldsymbol{u} = 0\,, \tag{2}$$

where $\boldsymbol{u}$ is the velocity field, p is the kinematic pressure, and ν is the kinematic viscosity. These equations need to be supplied with an initial condition for the velocity and a boundary condition. For the lid-driven cubic cavity flows, we will take as the simple homogeneous Dirichlet condition. The initial condition is zero velocity everywhere.

Time and Space Discretizations

In order to write the variational formulation of the finite element space discretization, let us introduce the forms:

$$a(\boldsymbol{u},\boldsymbol{v}) := \nu(\nabla\boldsymbol{u},\nabla\boldsymbol{v})\,,\ b(q,\boldsymbol{v}) := (q,\nabla\boldsymbol{v})\,,$$
$$c(\boldsymbol{u},\boldsymbol{v},\boldsymbol{w}) := (\boldsymbol{u}\cdot\nabla\boldsymbol{v},\boldsymbol{w})\,,$$

where $(\cdot,\cdot)$ denotes the standard L^2 inner product. In these expressions, $\boldsymbol{u},\boldsymbol{v},\boldsymbol{w}$ are assumed to belong to the velocity space $\boldsymbol{V} = \boldsymbol{H}_0^1(\Omega)$, and q belongs to the pressure space $Q = L^2(\Omega)$.

Having introduced these notations, the weak form of problem (Eq. 1~2) consists of finding $\boldsymbol{u}$ and p such that

$$(\partial_t\boldsymbol{u},\boldsymbol{v}) + c(\boldsymbol{u},\boldsymbol{u},\boldsymbol{v}) + a(\boldsymbol{u},\boldsymbol{v}) - b(p,\boldsymbol{v}) = 0 \quad \forall\boldsymbol{v}\in\boldsymbol{V}\,,$$
$$b(q,\boldsymbol{u}) = 0 \quad \forall q\in Q\,,$$

Monolithic time discretization, the generalized trapezoidal rule, is considered at first. Let $\theta\in[0,1]$ be a given parameter and consider a partition of $[0,T]$ into N time steps of equal size δt. Let f be a generic function of time and f^n the value of f at $t^n = n\delta t$, and let $f^{n+\theta} := \theta f^{n+1} + (1-\theta) f^n$, $\delta_t f^n := (f^{n+1} - f^n)/\delta t$. Given $\boldsymbol{u}^n$ at t^n, the time discrete problem consists of finding $\boldsymbol{u}^{n+1}$ and p^{n+1} at t^{n+1} as the solution of

$$(\delta_t\boldsymbol{u}^n,\boldsymbol{v}) + c(\boldsymbol{u}^{n+\theta},\boldsymbol{u}^{n+\theta},\boldsymbol{v}) + a(\boldsymbol{u}^{n+\theta},\boldsymbol{v}) - b(p^{n+1},\boldsymbol{v}) = 0 \quad \forall\boldsymbol{v}\in\boldsymbol{V}, \tag{3}$$

$$b(q,\boldsymbol{u}^{n+1}) = 0 \quad \forall q\in Q\,, \tag{4}$$

where $\theta = 1/2$ corresponds to the second-order Crank-Nicolson scheme, and $\theta = 1$ means the backward Euler method.

Let $\boldsymbol{V}_h$ be a finite element space to approximate $\boldsymbol{V}$, and Q_h a finite element space to approximate Q. We choose P1/P1 element pairs, which is stable when fractional step methods using a pressure Poisson equation are employed. Then the finite element discretization of Eq. 3 and Eq. 4 reads

$$\begin{aligned}&(\delta_t\boldsymbol{u}_h^n,\boldsymbol{v}_h) + c(\boldsymbol{u}_h^{n+\theta},\boldsymbol{u}_h^{n+\theta},\boldsymbol{v}_h)\\ &\quad + a(\boldsymbol{u}_h^{n+\theta},\boldsymbol{v}_h) - b(p_h^{n+\theta},\boldsymbol{v}_h) = 0 \quad \forall\boldsymbol{v}_h\in\boldsymbol{V}_h,\end{aligned} \tag{5}$$

$$b(q_h,\boldsymbol{u}_h^{n+1}) = 0 \quad \forall q_h\in Q_h\,, \tag{6}$$

The discrete version of the Eq. 5~6 can be rewritten as a coupled nonlinear algebraic system of the form

$$M\delta_t U^n + K(U^{n+\theta})U^{n+\theta} + GP^{n+1} = 0\,, \tag{7}$$

$$DU^{n+1} = 0\,, \tag{8}$$

where U and P are the arrays of nodal velocities and pressures, respectively, M is the mass matrix, K is the matrix containing the diffusive and convective parts, G is the gradient matrix, and D the divergence matrix.

Fractional Step Schemes

The fractional step schemes applied to the fully discrete problem (Eq. 7~8) is exactly equivalent to

$$M\frac{1}{\delta t}(\hat{U}^{n+1} - U^n) + K(U^{n+\theta})U^{n+\theta} + \gamma GP^n = 0\,, \tag{9}$$

$$M\frac{1}{\delta t}(U^{n+1} - \hat{U}^{n+1}) + G(P^{n+1} - \gamma P^n) = 0\,, \tag{10}$$

$$DU^{n+1} = 0\,, \tag{11}$$

where $\hat{U}^{n+1}$ is an auxiliary variable and γ is a numerical parameter, whose values are [0,1]. We make the essential approximation

$$K(U^{n+\theta})U^{n+\theta} \sim K(\hat{U}^{n+\theta})\hat{U}^{n+\theta}\,, \tag{12}$$

where $\hat{U}^{n+\theta} = \theta\hat{U}^{n+1} + (1-\theta)U^n$. If we write U^{n+1} in terms of $\hat{U}^{n+1}$ using Eq. 10 and inserting the result in Eq. 11, the equations to be solved are

$$M\frac{1}{\delta t}(\hat{U}^{n+1} - U^n) + K(\hat{U}^{n+\theta})\hat{U}^{n+\theta} + \gamma GP^n = 0\,, \tag{13}$$

$$\delta t DM^{-1}G(P^{n+1} - \gamma P^n) = D\hat{U}^{n+1}\,, \tag{14}$$

$$M\frac{1}{\delta t}(U^{n+1} - \hat{U}^{n+1}) + G(P^{n+1} - \gamma P^n) = 0\,, \tag{15}$$

which have been ordered according to the sequence of solution, for $\hat{U}^{n+1}$, P^{n+1} and U^{n+1}. We can approximate the operator $DM^{-1}G$ in Eq. 14 to the Laplace operator if M is approximated by a diagonal matrix. In this paper, $\gamma = 0.9$ and $\theta = 1$ are adopted.

Parallel Schemes

We consider solving in each time step a linearized form of systems, i.e. $Ax = y$, resulting from finite element discretization as described in the previous sections. Let Ω denote the computational mesh domain, and

$\{\Omega^i\}_{i=1}^{i=n}$ its decomposition into n non-overlapping sub-domains. Let $A_{LL} = diag[A_{11}, A_{22}, \cdots, A_{nn}]$ is a block-diagonal with each block $A_{ii}, i = 1, 2, \cdots, n$ being the matrix corresponding to the unknowns belonging to the interior vertices of sub-domain Ω_i . A_{LI} and A_{IL} represents connections between sub-domains to interfaces. A_{II} corresponds to the discretization of the differential operator restricted to the interfaces and represents the coupling between local interface points. Let $x = (x_L, x_I)^T$, $y = (y_L, y_I)^T$, then the linear system can be split to

$$\begin{pmatrix} A_{LL} & A_{LI} \\ A_{IL} & A_{II} \end{pmatrix} \begin{pmatrix} x_L \\ x_I \end{pmatrix} = \begin{pmatrix} y_L \\ y_I \end{pmatrix}. \tag{16}$$

The numerical solution of $Ax = y$ is equivalent to solving

$$(A_{II} - A_{IL} A_{LL}^{-1} A_{LI}) x_I = y_I - A_{IL} A_{LL}^{-1} y_L \,, \tag{17}$$

$$A_{LL} x_L = y_L - A_{LI} x_I \,. \tag{18}$$

The domain decomposition method starts by first determining x_I on the interfaces between sub-domains by solving Eq. 17. Upon obtaining x_I , the sub-domain problems (Eq. 18) decouple and may be solved in parallel.

RESULTS AND DISCUSSION

The computational model for 3D lid-driven cubic cavity flows is shown in Fig.1. The computational domain is $[0, 1] \times [0, 1] \times [0, 1]$. The lid of the cubic cavity moves parallel to the positive x -axis with the steady velocity $u = 1$. The other walls stay still. There is a reference pressure point of zero. The initial condition is zero velocity everywhere. The cubic cavity flow is dependent on the Reynolds number, which is determined by $\mathrm{Re} = Ud / \nu = 1/\nu$, where U is the velocity of the moving lid and d is the characteristic length of the cavity. So the kinematic viscosity ν is the pivotal parameter which determines the cavity flow features.

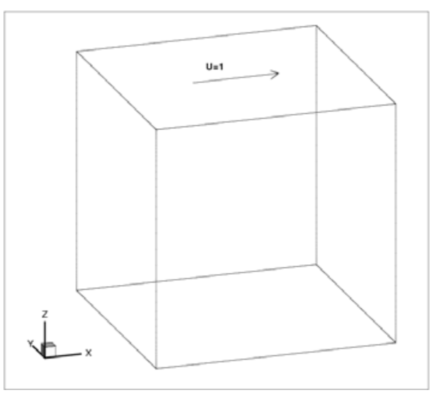

Fig. 1. The computational model for 3D lid-driven cubic cavity flows

The lid-driven cubic cavity flows at a series of Reynolds numbers ranging from 1 to 10000 are simulated, covering the steady field, unsteady laminar field and partly turbulent field. It is noted that all these flows are simulated with a uniform Cartesian $48 \times 48 \times 48$ mesh, while non-uniform meshes are widely used.

Lid-driven cubic cavity flow at Re=1000

For the cavity flow at Re=1000, a fixed time step of 0.05s is employed and 1000 iteration steps are performed. The lid velocity generates vorticity which propagates throughout until the flow field reaches a steady state. The 3D streamlines are illustrated in Fig. 2. From the side view, the downstream secondary eddy (DSE) and upstream secondary eddy (USE) can be observed clearly; from the back view, the flows in the DSE move from the symmetry plane to the side walls in spiral way, through the axis of the primary eddy back to the symmetry plane; from the oblique view, there are several streamlines from DSE, bottom wall, USE to the axis of the primary eddy, which form the corner eddies.

The iso-surfaces for different velocity magnitudes are shown in Fig. 3. As the flow moving through the cavity, the velocity magnitude decreases. With the influence of the side walls, the fluid accumulates near by the side walls. The accumulated fluid turns to the central part, and then moves forward in a spiral way, which forms the corner eddies. Fig. 3(d) suggests that the corner eddies propagate throughout the whole cavity. As shown in Fig. 3 (b) and (c), the jet flow near the symmetry plane is accelerated by impinging the bottom wall and the upstream wall.

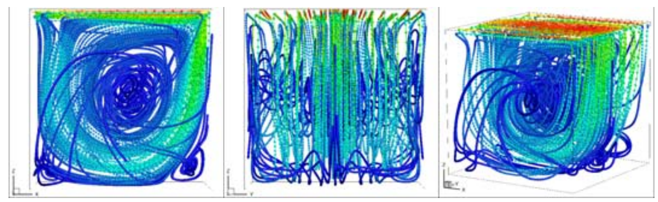

(a) (b) (c)

Fig. 2. 3D streamlines at Re=1000 on different views: (a) side view; (b) back view; (c) oblique view.

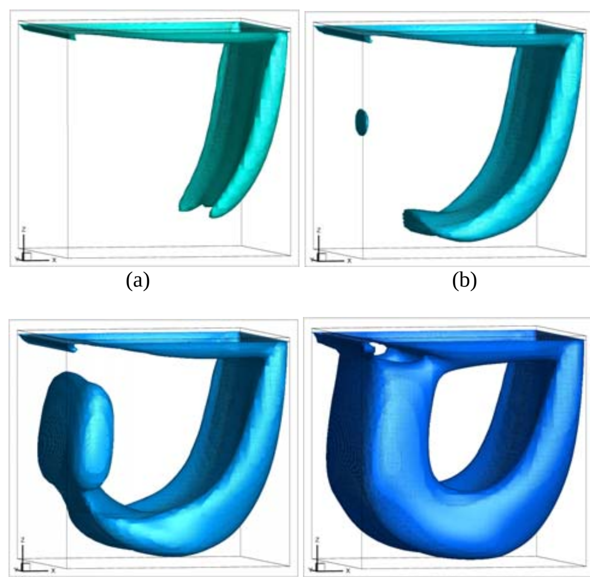

(c) (d)

Fig. 3. Iso-surfaces for different velocity magnitudes at Re=1000: (a) 0.3; (b) 0.25; (c) 0.2; (d) 0.15.

Iso-surfaces of the pressure and ω_y are illustrated in Fig. 4. With the effect of the side walls, these iso-surfaces are visualized with 3D properties.

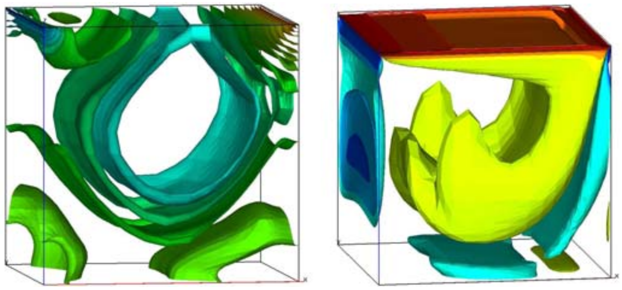

(a) (b)

Fig. 4. Iso-surfaces for different variables at Re=1000: (a) pressure; (b) y-component of the vorticity, i.e. ω_y .

The u -velocity component profile along the vertical centerline in the symmetry plane has been used as a measure of solution accuracy for the 3D lid-driven cavity benchmark. The computed solution from the present formulation is shown in Fig. 5, which coincides well with the one given by Wong *et al*. (2002).

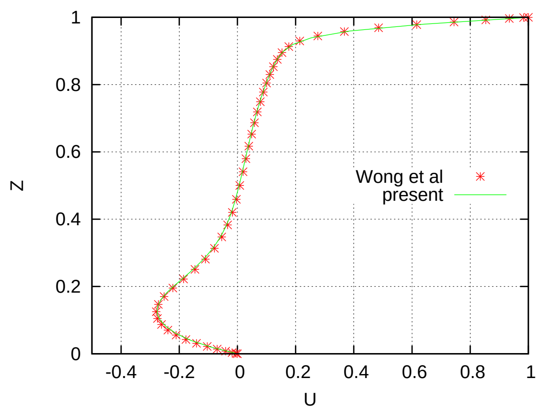

Fig. 5. u -velocity profile comparison along the vertical centerline in the symmetry plane at Re=1000.

Lid-driven cubic cavity flows at low Reynolds numbers

In this subsection, cavity flows at Re=1, 10, 100, and 400 are simulated. These flows are laminar steady state. As shown in Fig. 6, the kinematic energy of the whole cavity is enhanced with the increase of the Reynolds number. Cavity flows have 3D properties even when Re is very small.

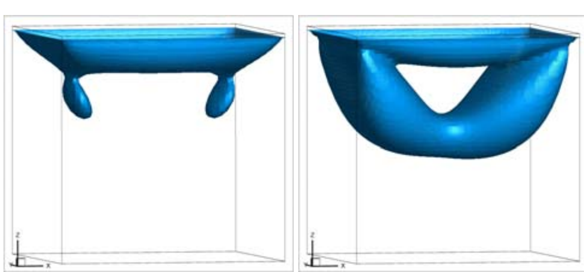

(a) (b)

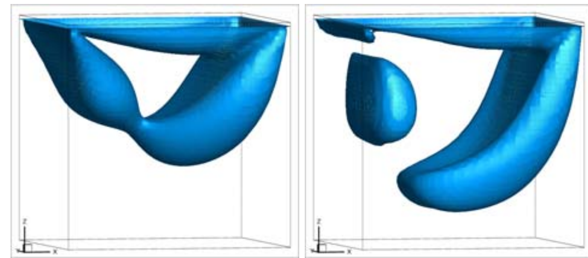

(c) (d)

Fig. 6. Iso-surfaces of velocity magnitude of 0.2 for different Reynolds numbers: (a) Re=1; (b) Re=10; (c) Re=100; (d) Re=400.

The 3D sectional perspective views for the computed velocity vector and vorticity fields at Re=400 is shown in Fig. 7. The vorticity plots at x=0.5 for ω_x , y=0.5 for ω_y , and z=0.5 for ω_z fully illustrate the transport of flow information. The streamlines projection shows the secondary flows and corner eddies clearly. These results are very similar with the ones given by Wong *et al*. (2002).

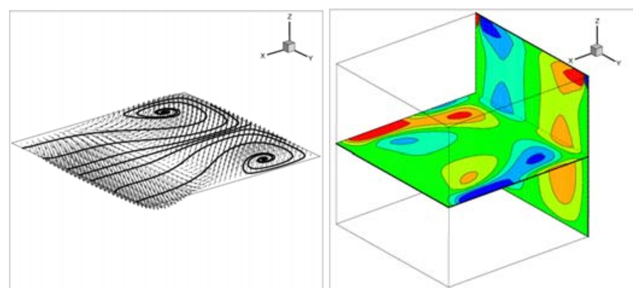

(a) (b)

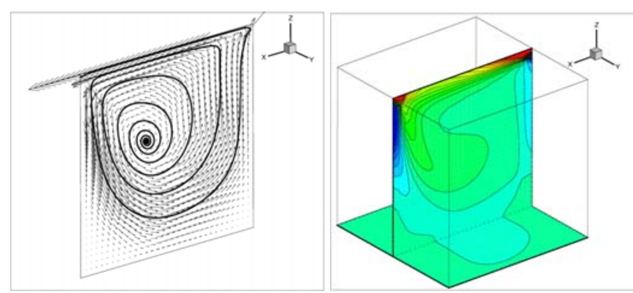

(b) (d)

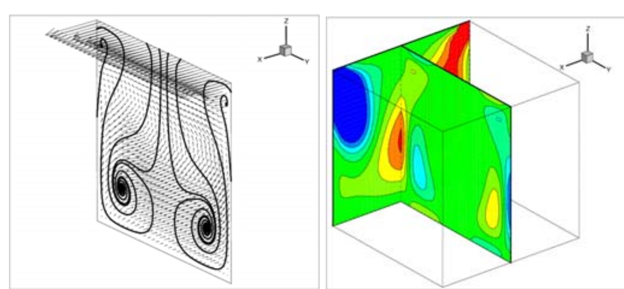

(e) (f)

Fig. 7. Perspective 3D solution summary at Re=400: (a) streamlines projection at z=0.5; (b) ω_z ; (c) streamlines projection at y=0.5; (d) ω_y ; (e) streamlines projection at x=0.5; (f) ω_x .

Fig. 8 indicate that the secondary flows and corner eddies are always exist with the influence of the side walls, although the vorticity is not so strong at small Reynolds numbers. Cubic cavity flows have intrinsic 3D features.

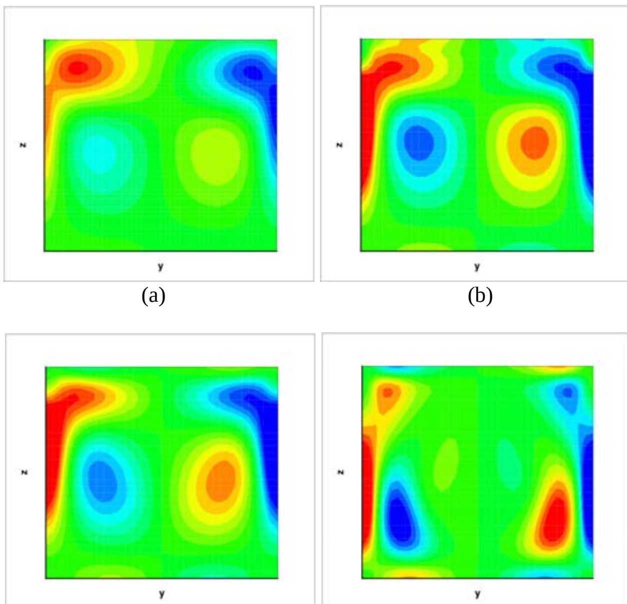

Fig. 8. ω_x at x=0.5 for different Reynolds numbers: (a) Re=1, $\omega_x \in$ [-0.005, 0.005]; (b) Re=10, $\omega_x \in$ [-0.05, 0.05]; (c) Re=100, $\omega_x \in$ [-0.5, 0.5]; (d) Re=400, $\omega_x \in$ [-1, 1].

2D planar projections of the velocity vector field at Re=100, 400, and 1000 on the three centroidal planes of the cube are shown in Fig. 9. As can be seen at y=0.5, the center of the primary eddy starts in the upper right half region, then gradually moves toward the cube center as the Reynolds number increases. At x=0.5 plane, a pair of vortices appear near the centerline and move out towards the lower corners as the Reynolds number increases. Two small eddies are also emerging at the top corners as the Reynolds number goes through 400 to 1000. At z=0.5 plane, corner eddies can be seen as well.

The computed u -velocity profile along the vertical centerline in the symmetry plane at Re=100 and 400 are compared with the reference results respectively, which are shown in Fig. 10 and Fig. 11. The present solutions match well with other numerical results.

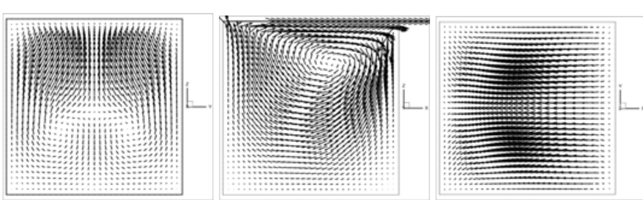

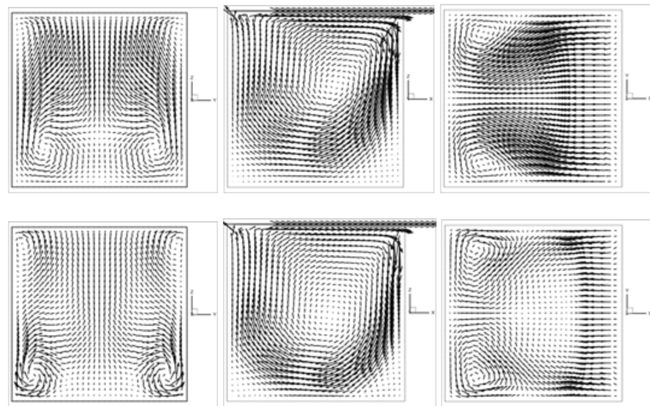

Fig. 9. 2D planar projections of mid-plane velocity vector for different Reynolds number: Re=100 (top); Re=400 (middle); Re=1000 (bottom) on different planes: x=0.5 (left); y=0.5 (middle); z=0.5 (right).

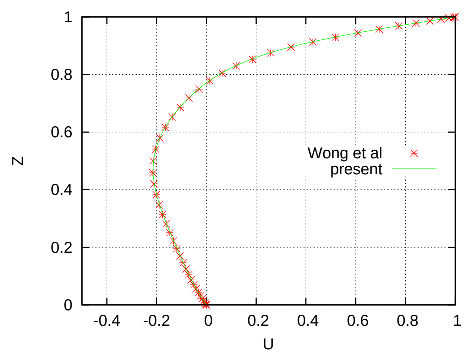

Fig. 10. u -velocity profile comparison along the vertical centerline in the symmetry plane at Re=100.

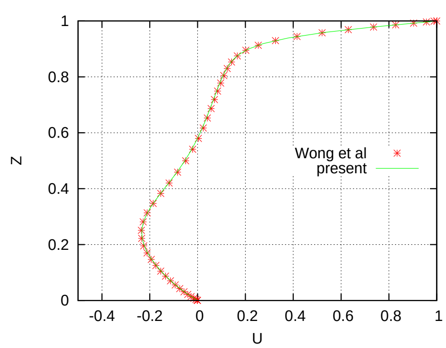

Fig. 11. u -velocity profile comparison along the vertical centerline in the symmetry plane at Re=400.

Lid-driven cubic cavity flows at moderate Reynolds numbers

Moderate Reynolds number 2000 and 3200 are selected for the simulations of cubic cavity flows. These flows are unsteady but laminar. A fixed time step of 0.05s is employed. The total simulation time is 1000s with the last 500s utilized for collecting flow statics.

Taylor-Gortler-like (TGL) vortices are observed at Re=2000 and 3200.

These vortices are caused due to centrifugal forces, when the flow moves along the curvature formed by downstream wall, downstream secondary eddies, and bottom wall. These longitudinal vortices take part in a slow spanwise motion quasi-periodically. A quasi-periodic evolution of TGL vortices at Re=2000 is illustrated in Fig. 12. As can be seen, there are two pairs of TGL vortices besides corner eddies. The evolution procedure seems to be: the left pair vortices become stronger and move to the centerline slowly, while the right pair becoming weaker; the left pair vortices disappear when they reach the centerline, while a new pair emerging near the left corner; then the right pair vortices become stronger and move to the centerline as the left pair have done; after the right pair vortices disappear and reborn, the procedure goes into the next period. The time of one period is approximate 60s.

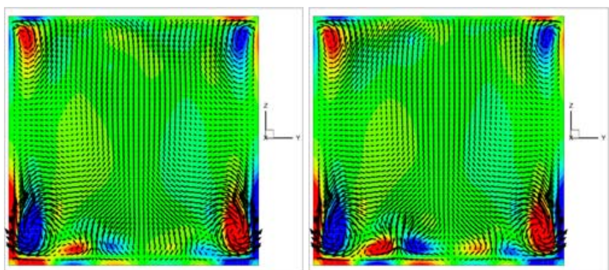

(a) (b)

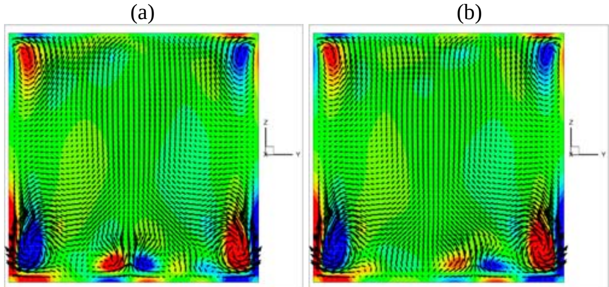

(c) (d)

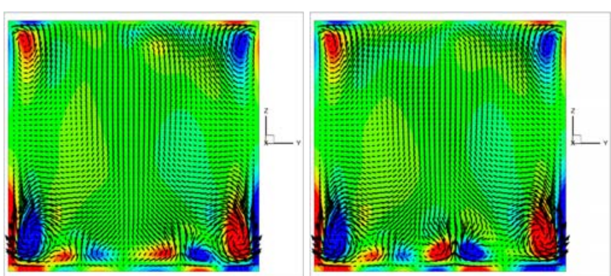

(e) (f)

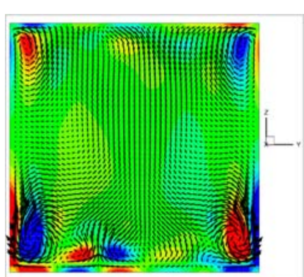

(g)

Fig. 12. The evolution of TGL vortices at Re=2000 (x=0.5): (a) t=340s; (b) t=350s; (c) t=360s; (d) t=370s; (e) t=380s; (f) t=390s; (g) t=400s.

3D streamlines at Re=3200 are presented in Fig. 13. From the side view, the DSE and USE are smaller than which at Re=1000; from the back view, the DSE is of asymmetry and irregular which affected by TGL vortices.

A series of experiments has been conducted in a lid-driven cavity at Reynolds numbers between 3200 and 10000 by Prasad & Koseff (1989). The mean and root-mean-square velocities profiles along the horizontal and vertical centerlines in the symmetry plane of this work are shown in Fig. 14, which are compared to the experiment data. It is noted that the experiment has accumulated 5.46 min (~327s) of velocity data at each measuring point, while 500s values are collected for our statistics. However, as you can see, the mean velocities profiles coincide with experiment data, and the root-mean-square (rms) velocities profiles keep reasonable agreement with experiment one. The root-mean-square (rms) velocities are very important statistics to measure the fluctuations of the velocities for the unsteady flow. As shown in Fig. 14(c), Urms are larger near the lid and the bottom wall than which in the cavity center, because of the influence of the boundary layers; Urms are larger near the bottom wall than which near the lid, because the DSE and the TGL vortices are strongly unsteady; there is a secondary peak value of the Urms near the bottom wall, which is due to the fluctuations of the TGL vortices. Similar statistics profile can be seen in Fig. 14(d), while the TGL vortices appear near the upstream wall (x=0). Wrms are larger near the downstream wall (x=1) than which near the upstream wall, because the peak value of the mean velocity <W> near the downstream wall is twice of the one near the upstream wall, and the DSE is much more unstable than the USE.

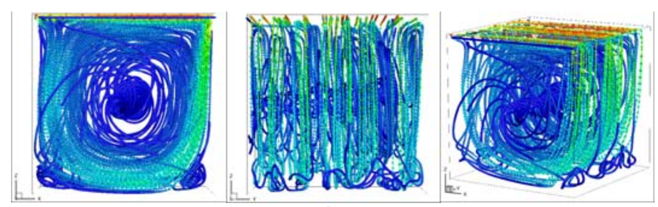

(a) (b) (c)

Fig. 13. 3D streamlines at Re=3200 on different views: (a) side view; (b) back view; (c) oblique view.

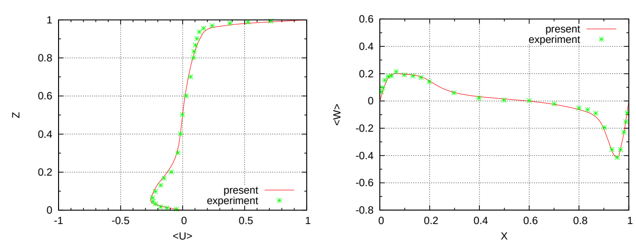

(a) (b)

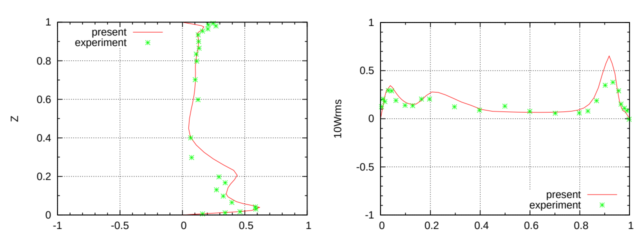

(c) (d)

Fig. 14. The mean and root-mean-square velocity statistics comparison along the horizontal and vertical centerlines in the symmetry plane at Re=3200: (a) <U>; (b) <W>; (c) 10Urms; (d) 10Wrms.

Lid-driven cubic cavity flows at high Reynolds number

Cavity flow at Re=10000 is simulated in this subsection, which is partly turbulent. The solution at Re=3200 is used as the initial data for this simulation. A fixed time step of 0.02s is employed. The total simulation time is 800s with the last 400s utilized for collecting flow statics.

Fig. 15 shows the 3D streamlines sometime on different views. From the side view, the DSE and USE occupy small spaces; from the back view, the streamlines in DSE are irregular, almost random, which affect the streamlines along the downstream wall as well.

As similar as the case at Re=3200, the mean and root-mean-square velocities profiles are shown in Fig. 16. It is noted that we collect 400s values for statistics, while the experiment has accumulated 5.46 min (~327s). As can be seen, the mean and mean-root-square velocities profiles keep reasonable agreement with experiment data respectively. As shown in Fig.15 and 16, the peak values of the mean velocity <U> and <W> at Re=10000 is smaller than which at Re=3200, while the root-mean-square velocities at Re=10000 are larger respectively. The cavity flow at Re=10000 is partly turbulent, so the boundary layers are thinner than the laminar flow, the momentum and energy exchanges between the boundary layers and central part are much stronger, and the velocities display much larger and more random fluctuations at high frequencies. The secondary peak values of the rms velocities profiles are not clear in Fig. 16. This suggests that the high frequency fluctuations are dominant and that they have destroyed the integrity of the TGL vortices.

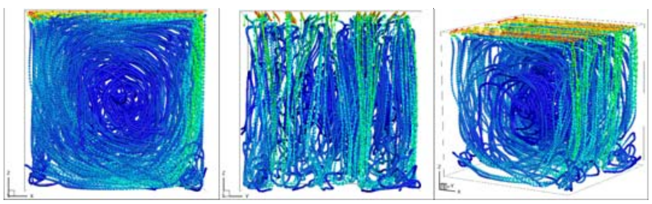

(a) (b) (c)

Fig. 15. 3D streamlines at Re=10000 on different views: (a) side view; (b) back view; (c) oblique view.

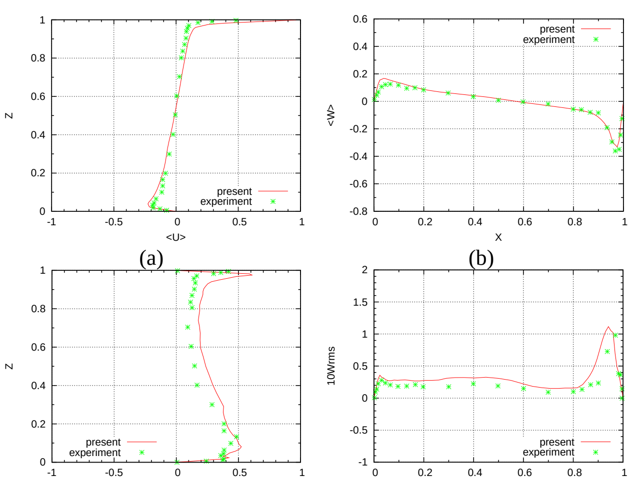

(a) (b) (c) (d)

Fig. 16. The mean and root-mean-square velocity statistics comparison along the horizontal and vertical centerlines in the symmetry plane at Re=10000: (a) <U>; (b) <W>; (c) 10Urms; (d) 10Wrms.

Parallel implementation performance

Mesh domain decomposition method with MPI are implemented for the parallel computation. First, the whole mesh is decomposed to several non-overlapping sub-domains by the open source software METIS. Fig. 17 shows the mesh decomposition for different sub-domains. As can be seen, the balance of sub-domains is kept well. Each sub-domain is assigned to a processor on the Intel(R) Xeon(R) CPU of 2.27GHz. The information of the interface among the sub-domains is passed among the processors by MPI.

All the cases mentioned above are simulated with 8 processors. For the parallel performance test, we compute cavity flows at Re=3200 with different processors from 1 to 8. A fixed time step of 0.05s and 1000 iteration steps are implemented in the test case. Parallel performance, including time and speedup ratio, is shown in Fig. 18. As can be seen, computation time decreases and speedup ratio increases as the number of processors increases. The speedup ratio is smaller than the linear one because of the time consuming of the increasing message passing.

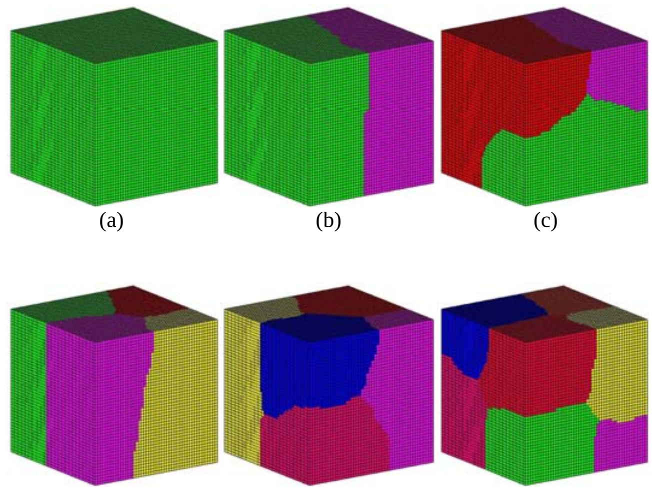

(a) (b) (c) (d) (e) (f)

Fig. 17. Mesh decomposition for different sub-domains: (a) 1; (b) 2; (c) 3; (d) 4; (e) 6; (f) 8.

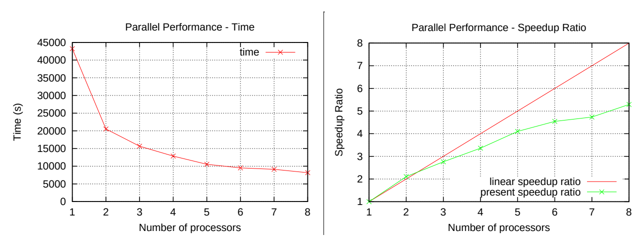

(a) (b)

Fig. 18. Parallel performance at Re=3200: (a) time; (b) speedup ratio.

CONCLUSIONS

The fractional step finite element method is applied to solve the incompressible viscous fluid problems. Mesh domain decomposition method with MPI technique is implemented to parallel simulate the 3D lid-driven cubic cavity flows at the Reynolds numbers between 1 and 10000, covering the steady field, unsteady laminar field and partly turbulent field. At low Reynolds numbers, intrinsic 3D properties such as corner eddies are illustrated. The present velocity profiles along the vertical centerline in the symmetry plane at Re=100, 400, and 1000 agree well with other numerical solutions respectively. At moderate Reynolds numbers (2000 and 3200), a quasi-periodic evolution of the TGL vortices is presented. At high Reynolds number (10000), the mean and mean-root-square velocities statistics along the horizontal and vertical centerlines in the symmetry plane keep reasonable agreement with experiment data respectively. Parallel time consuming and speedup ratio are presented to show the good parallel performance.

From these results, it is found that the complex 3D lid-driven cubic cavity flows can be efficiently and reasonably simulated by solving the Navier-Stokes equations based on the tools of PETScFEM. The PETScFEM is not only an efficient CFD tool, but also lays a good basis for constructing new numerical methods and schemes.

ACKNOWLEDGEMENTS

The support of National Natural Science Foundation of China (Grant No. 11072154, 50739004), Research Foundation of State Key Laboratory of Ocean Engineering of China (Grant No. GKZD010064) and the Program for Professor of Special Appointment (Eastern Scholar) at Shanghai Institutions of Higher Learning for this work is gratefully acknowledged.

REFERENCES

Bessonov, O, Brailovskaya, V, Polezhaev, V, and Roux, B (1995). “Parallelization of the Solution of 3D Navier-Stokes Equations for Fluid Flow in a Cavity with Moving Covers,” *Parallel Computing Technologies*, Vol 964, pp 385-399.

Bouffanaisa, R, and Devilleb, MO (2007). “Large-eddy simulation of the flow in a lid-driven cubical cavity,” *Physics Of Fluids*, Vol 19, pp 055108.

Bouffanaisa, R, Devilleb, MO, Fischer, PF, Leriche, E, and Weill, D (2006). “Large-eddy simulation of the lid-driven cubic cavity flow by the spectral element method,” *J Sci Comput*, Vol 27, No 1, pp 51-62.

Chiang, TP, Hwang, RR, and Sheu, WH (1996). “Finite Volume Analysis Of Spiral Motion In A Rectangular Lid-Driven Cavity,” *International Journal For Numerical Methods In Fluids*, Vol 23, pp 325-346.

Chiang, TP, and Sheu, WH (1997). “Numerical prediction of eddy structure in a shear-driven cavity,” *Computational Mechanics*, Vol 20, pp 379-396.

Chiang, TP, Sheu, WH, and Hwang, RR (1998). “Effect Of Reynolds Number On The Eddy Structure In A Lid-Driven Cavity,” *International Journal For Numerical Methods In Fluids*, Vol 26, pp 557 -579.

Codina, R (2001). “Pressure Stability in Fractional Step Finite Element Methods for Incompressible Flows,” *Journal of Computational Physics*, Vol 170, No 1, pp 12-40.

Deshpande, MD, and Milton, SG (1998). “Kolmogorov scales in a driven cavity flow,” *Fluid Dynamics Research*, Vol 22, No 3, pp 59-81.

Feldmana, Y, and Gelfgat, AY (2010). “Oscillatory instability of a three-dimensional lid-driven flow in a cube,” *Physics Of Fluids*, Vol 22, pp 093602.

Guermond, JL, and Quartapelle, L (1998). “On stability and convergence of projection methods based on pressure poisson equation,” *Int J Numer Meth Fluids*, Vol 26, pp 1039-1053.

Hachem, E, Rivaux, B, Kloczko, T, Digonnet, H, and Coupez, T (2010). “Stabilized finite element method for incompressible flows with high Reynolds number,” *Journal of Computational Physics*, Vol 229, No 8, pp 643-665.

Jiang BN, Lin TL, Povinelli LA (1994). “Large scale computation of incompressible viscous flows by least-squares finite element method,” *Computer Methods in Applied Mechanics and Engineering*, Vol 114, No 3-4, pp 213-231.

Kreizer, M, Ratner, D, and Liberzon, A (2010). “Real-time image processing for particle tracking velocimetry,” *Exp Fluids*, Vol 48, No 1, pp 105-110.

Leriche, E (2006). “Direct Numerical Simulation in a Lid-Driven Cubical Cavity at High Reynolds Number by a Chebyshev Spectral Method,” *Journal of Scientific Computing*, Vol 27, No 1-3, pp 335-345.

Lerichea, E, and Gavrilakis, S (2000). “Direct numerical simulation of the flow in a lid-driven cubical cavity,” *Physics Of Fluids*, Vol 12, No 6, pp 1363.

Paz, RR, Nigro, NM, Storti. MA (2006). “On the efficiency and quality of numerical solutions in CFD problems using the Interface Strip Preconditioner for domain decomposition methods,” *Int J Numer Meth Fluids*, Vol 52, No 1, pp 89-118.

Prasad, AK, and Koseff, JR (1989). “Reynolds number and end-wall effects on a lid-driven cavity flow,” *Phys Fluids*, Vol 1, No 2, pp 208.

Rhee, HS, Koseff, JR, and Street, RL (1984). “Flow visualization of a recirculating flow by rheoscopic liquid and liquid crystal techniques,” *Experiments in Fluids*, Vol 2, pp 57-64.

Ryu, YH, and Baik, JJ (2009). “Flow and dispersion in an urban cubical cavity,” *Atmospheric Environment*, Vol 43, No 1, pp 721-729.

Shankar, PN, and Deshpande, MD (2000). “Fluid Mechanics in The Driven Cavity,” *Annu Rev Fluid Mech*, Vol 32, pp 93-36.

Shetty, DA, Fisher, TC, Chunekar, AR, and Frankel, SH (2010). “High-order incompressible large-eddy simulation of fully inhomogeneous turbulent flows,” *Journal of Computational Physics*, Vol 229, No 8, pp 802-822.

Sonzogni, VE, Yommi, AM, Nigro, NM, Storti. MA (2002). “A parallel finite element program on a Beowulf cluster,” *Advances In Engineering Software*, Vol 33, No 7-10, pp 427-443.

Tai, CH, Zhao, Y, and Liew, KM (2005). “Parallel-multigrid computation of unsteady incompressible viscous flows using a matrix-free implicit method and high-resolution characteristics-based scheme,” *Comput Methods Appl Mech Engrg*, Vol 194, No 3, pp 949-983.

Verstappen, RWCP, and Veldman, AEP (1997). “Direct numerical simulation of turbulence at lower costs,” *Journal of Engineering Mathematics*, Vol 32, No 1, pp 43-59.

Wong, KL, and Baker, AJ (2002). “A 3D incompressible Navier-Stokes velocity-vorticity weak form finite element algorithm,” *Int J Numer Meth Fluids*, Vol 38, No 9, pp 9-23.

Zang, Y, Street, RL, and Koseff, JR (1993). “A dynamic mixed subgrid-scale model and its application to turbulent recirculating flows,” *Phys Fluids*, Vol 5, No 12, pp 3186.